Assessment of a fully 3D Monte Carlo reconstruction method for preclinical PET with iodine-124

2015 Phys. Med. Biol. 60 2475

(http://iopscience.iop.org/0031-9155/60/6/2475)

IOP Publishing | Institute of Physics and Engineering in Medicine Physics in Medicine & Biology

Phys. Med. Biol. **60** (2015) 2475–2491 doi:10.1088/0031-9155/60/6/2475

Assessment of a fully 3D Monte Carlo reconstruction method for preclinical PET with iodine-124

M Moreau[1,2], I Buvat[3], L Ammour[4], N Chouin[2,4], F Kraeber-Bodéré[1,4], M Chérel[1] and T Carlier[1,4]

[1] CRCNA, INSERM, University of Nantes, UMR 892, Nantes, France
[2] AMaROC, National Veterinary School ONIRIS, Nantes, France
[3] I2BM, CEA-SHFJ, Orsay, France
[4] Nuclear Medicine Department, University Hospital of Nantes, Nantes, France

E-mail: thomas.carlier@chu-nantes.fr

Received 22 September 2014, revised 30 January 2015
Accepted for publication 3 February 2015
Published 5 March 2015

Abstract

Iodine-124 is a radionuclide well suited to the labeling of intact monoclonal antibodies. Yet, accurate quantification in preclinical imaging with I-124 is challenging due to the large positron range and a complex decay scheme including high-energy gammas. The aim of this work was to assess the quantitative performance of a fully 3D Monte Carlo (MC) reconstruction for preclinical I-124 PET. The high-resolution small animal PET Inveon (Siemens) was simulated using GATE 6.1. Three system matrices (SM) of different complexity were calculated in addition to a Siddon-based ray tracing approach for comparison purpose. Each system matrix accounted for a more or less complete description of the physics processes both in the scanned object and in the PET scanner. One homogeneous water phantom and three heterogeneous phantoms including water, lungs and bones were simulated, where hot and cold regions were used to assess activity recovery as well as the trade-off between contrast recovery and noise in different regions. The benefit of accounting for scatter, attenuation, positron range and spurious coincidences occurring in the object when calculating the system matrix used to reconstruct I-124 PET images was highlighted. We found that the use of an MC SM including a thorough modelling of the detector response and physical effects in a uniform water-equivalent phantom was efficient to get reasonable quantitative accuracy in homogeneous and heterogeneous phantoms. Modelling the phantom heterogeneities in the SM did not necessarily yield the most accurate estimate of the activity distribution, due to the high variance affecting many SM elements in the most sophisticated SM.

Keywords: PET, iodine-124, Monte Carlo, reconstruction, system matrix

S Online supplementary data available from stacks.iop.org/PMB/60/062475

(Some figures may appear in colour only in the online journal)

1. Introduction

For more than two decades, monoclonal antibodies (MAbs) have been labeled with gamma-emitting radionuclides and subsequently used in planar or single photon emission tomography (Herbertson *et al* 2014, Lütje *et al* 2014). However, absolute quantification might be easier using MAbs positron emission tomography (PET), called immuno-PET (Poli *et al* 2013). In that context, Iodine-124 (^{124}I) is well suited to the labeling of large molecules such as intact MAbs (Knowles and Wu 2012, Wright and Lapi 2013). In radioimmunotherapy involving α-emitters, ^{124}I could be a substitute to astatine-211 for biodistribution and dosimetric studies, since the stability of the labeling is similar for these two radionuclides (Walte *et al* 2007).

Quantitative ^{124}I PET has been previously investigated in clinical (Vandenberghe *et al* 2006b, Herzog *et al* 2008, Gregory *et al* 2009, Jentzen *et al* 2010) and preclinical settings (Yao *et al* 2005, Sauerzapf *et al* 2011, Taleb *et al* 2012). Yet, accurate quantification in preclinical imaging with ^{124}I remains challenging due to the large positron range (maximum energy: 1.5 MeV (11.5%) and 2.1 MeV (11.5%), as compared to 0.6 MeV for ^{18}F) worsening the spatial resolution, and to a complex decay scheme including high-energy gamma (~60% at 603 keV and ~10% at 723 keV) partly emitted in cascade with the positrons (Disselhorst *et al* 2010). The cascade decays can produce non-annihilation true coincidences, called cascade-coincidences in this paper, when a high-energy photon creates a coincidence with a 511 keV photon. These cascade-coincidences contribute to the background activity in clinical (Surti *et al* 2009) and preclinical (Herzog *et al* 2002) settings, with a fraction of ~35% of the total measured coincidences when using a preclinical PET system (Yu *et al* 2009).

Several groups have already tackled issues that are of foremost importance in ^{124}I PET. Methods have been proposed to account for the positron range within the reconstructed algorithm for high energetic positrons (Rahmim *et al* 2013). Rahmim *et al* (2008a) described a space-invariant correction involving a 3D bi-exponential modelling of the annihilation distribution in a homogeneous media. Monte Carlo (MC) simulations have also been used to determine the convolution kernels to be introduced in the forward step of an OSEM (ordered subset expectation maximization) algorithm (Cal-Gonzalez *et al* 2009) or in the forward and back-projection steps using a MAP (maximum a posteriori) algorithm (Ruangma *et al* 2006). In addition, few studies used a truncated convolution kernel calculated in water to account for the soft tissue/air boundary (Bai *et al* 2003, Bai *et al* 2005). However, while an improvement in spatial resolution has been reported, these approaches may introduce artifacts in reconstructed images. Space-variant modelling of the annihilation distribution was also considered in heterogeneous media. One possibility is to compute the annihilation distribution for few materials in the human body (such as water, lung an bone) and take advantage of the CT scan to determine the annihilation distribution within different media (Alessio *et al* 2008, Rahmim *et al* 2008b). Quantitative improvements compared with a space-invariant positron range model strongly depend on the heterogeneities present in the propagation medium. Last, the use of MC simulations within the reconstruction for determining the annihilation distribution in heterogeneous media has been investigated but is computationally intensive (Fu and Qi 2010).

The spatially uncorrelated cascade-coincidences produce a slowly varying background activity in the sinogram. This background activity can be estimated and subsequently subtracted

from the initial sinogram. The estimation can be based on fitting the sinogram tails with either a uniform (Pentlow *et al* 2000), linear (Lubberink *et al* 2002) or quadratic (Kull *et al* 2004) function. Another approach estimates the cascade-coincidences sinogram using a spatially variant convolution-subtraction technique (Beattie *et al* 2003, Walrand *et al* 2003). In this approach, the cascade-coincidence sinogram results from the convolution of an analytically-computed kernel with an ideal activity distribution (i.e. without scatter nor attenuation). Alternatively, an approach similar to the single scatter simulation correction developed by Watson *et al* (2000) for scattered coincidences can be used (Cheng *et al* 2009, 2011, Laforest and Liu 2009). However, these methods require an initial estimate of the activity distribution. This estimate is usually obtained from a 2D analytical reconstruction of the original sinogram corrected for scatter and attenuation and assuming a uniform background subtraction for cascade distribution correction.

The full MC modelling of the system matrix (SM) used in iterative reconstruction makes it possible to precisely account for all physical effects occurring in the scanner and the object (Floyd *et al* 1986, Veklerov *et al* 1988). This approach was already investigated in SPECT accounting for the object and scanner (Lazaro *et al* 2005, Aguiar *et al* 2014). The performance of this approach in PET imaging relies partly on the accuracy of the SM elements R_{ij}, where each R_{ij} is the probability that an event emitted from a source voxel j in the object is assigned to a specific LOR i. Yet, when particle-matter interactions in the object are considered, the prohibitive MC modelling time is the main limitation of this approach. Up to now, when using a MC calculation of the SM in PET imaging, only the point spread function (PSF) of the detector has been modeled (Rafecas *et al* 2004, Vandenberghe *et al* 2006a, Aguiar *et al* 2010, Ortuño *et al* 2010, Cabello and Rafecas 2012) and the associated SM was sparse (Kontaxakis *et al* 2002). By taking advantages of the SM sparsity and of scanner symmetries, simulation time and memory requirement could be reduced (Johnson *et al* 1995).

It is also possible to factorize the SM as a product of independent contributions (geometry, particle interactions in the detectors and in the object) to reduce its size, and allow for an independent computation of each contribution (Qi *et al* 1998, Rahmim *et al* 2008a, Cecchetti *et al* 2013). However, these techniques often require simplifications since the SM can usually not be written as a product of sparse diagonal matrices (Ortuño *et al* 2010). For instance, there is no model in which the accolinearity effect is independent from the geometric projector.

The aim of this work was to assess the quantitative performance of a fully 3D MC reconstruction for preclinical ^{124}I PET. We investigated the benefits of using a complete description of the physics processes both in the PET scanner and in the object for calculating the SM and assessed the impact of different level of complexity and statistical properties of the SM on the resulting image features.

2. Methods

2.1. PET system

The high-resolution small animal Inveon PET system from Siemens was used. This scanner consists of 64 blocks of 20 × 20 lutetium-oxyorthosilicate (LSO) crystals (1.51 × 1.51 × 10 mm^3) readout by position sensitive photomultipliers tubes. The 25 600 crystals arranged in 16 modules of 4 blocks and 80 axial rings yield ~164 millions lines of response (LOR). The transaxial field of view (FOV) is 10.0 cm in diameter and the axial FOV is 12.7 cm.

2.2. Simulated acquisitions

A homogeneous thin water phantom P0 (30 × 30 × 2 mm^3, voxel size: 1 × 1 × 1 mm^3) with hot and cold inserts in a background was used: the hot and cold regions were 8 × 8 × 2 mm^3

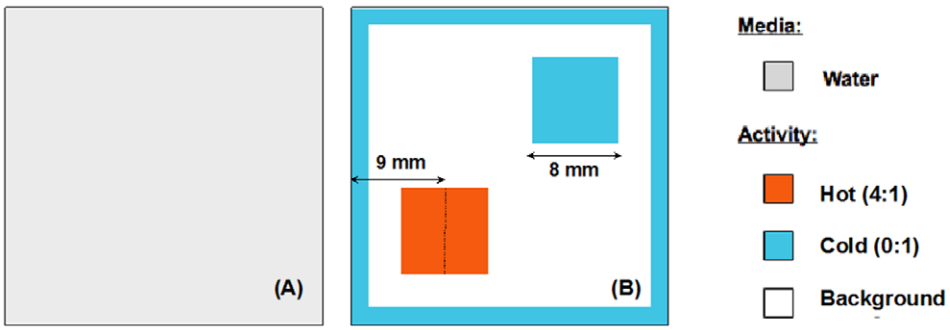

Figure 1. Axial slice of phantom P0: medium (*a*) and activity distribution (*b*).

(figure 1). Hot and background regions were filled with ^{124}I source. The activity concentration in the hot region was 4 times the activity within the background, while the cold region contained no activity. The background activity was only filled in the 26 × 26 × 2 centered voxels. The simulations were performed with GATE v6.1 (Jan *et al* 2011).

A heterogeneous phantom (30 × 30 × 2 mm^3, voxel size: 1 × 1 × 1 mm^3) composed of water, lung and bone (figure 2(*a*)) was also designed to produce three groups of heterogeneous projections.

Phantom P1 was filled with ^{124}I as shown in figure 2(*b*). In phantom P2, five hot regions mimicking tumors were added with dimensions ranging from 1 × 1 to 5 × 5 mm^2. The 'tumors' were located near the bone (figure 2(*c*)) and also filled with ^{124}I.

PET acquisitions were simulated so that the number of detected prompts was similar for all settings (2.32 × 10^6 for P0, 2.72 × 10^6 for P1 and 2.35 × 10^6 for P2).

2.3. System matrix computation

Given the simulated phantom and cylindrical geometry of the pre-clinical PET scanner, we took advantage of the symmetries in the phantom and in the PET system for reducing the number of particles needed for SM computation. Considering a transaxial plane in the Inveon FOV and the voxelized phantom in the center of the FOV, eight symmetries were used for voxels with the same x and y coordinates in the transaxial planes and sixteen symmetries for all others. As a result, only 7% of the initial volume was used for computing the different SM. Only non-zero elements of the SM were stored.

For each phantom, three different SMs were calculated to investigate the benefit of using a complete description of the physical processes for calculating the SM.

The first SM was created by simulating photon pairs in opposite directions (*Back-To-Back* source in GATE). Interactions in the object were not modeled as if photons propagated in vacuum. Only the system geometry and photon interactions in the PET system (crystal scattering and penetration) were modeled. This model was called *BtB-Vacuum* and the resulting SM modelling only the PSF of the scanner was used for all phantoms.

The second SM was calculated by simulating a ^{124}I source. The interactions in the object were explicitly modeled assuming the phantoms consisted of water only (instead of soft tissue, lung or bone encountered in real animals). This second SM accounted for attenuation, scatter, positron range and spurious coincidences (511 keV photon in coincidence with a gamma photon emitted in cascade) as occurring in a water medium. Cascade-γ of ^{124}I were included

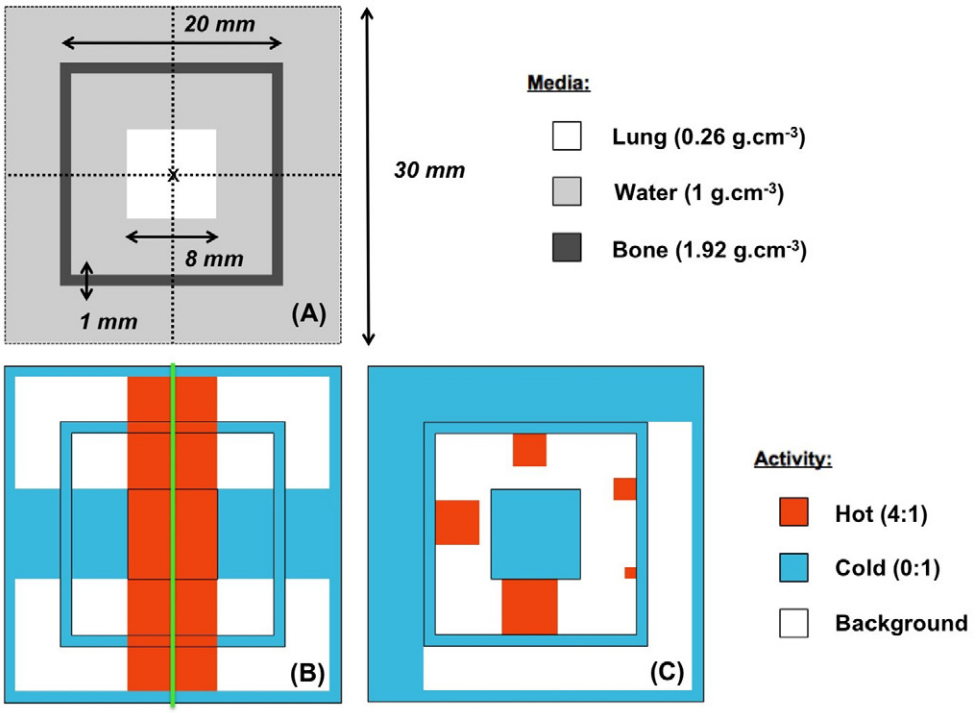

Figure 2. Description of phantoms P1 (*b*) and P2 (*c*) involving a heterogeneous medium (*a*). The green line (*b*) shows the location of the profile measured across the hot region.

because of the linear relationship between simulated activity and the number of coincidences involving cascade-γ. This model was called I124-*Uniform* and the resulting SM was used for all three phantoms described in section 2.2.

The third type of SMs was identical to I124-*Uniform* SM except that the medium heterogeneity was taken into account (water, lung and bone). This model was called I124-*Real*. Note that the object used to calculate I124-*Uniform* SM and I124-*Real* SM had the dimensions and composition of phantoms P1 and P2 described in the section 2.2.

Each of these SMs was computed with different statistical variances in the SM elements leading to 12 SMs, as shown in table 1.

Note that *BtB-Vacuum Large*, I124-*Uniform Large* and I124-*Real Small* SM have approximately (6% maximum difference) the same number of detected coincidences for comparison purpose. Therefore, *BtB-Vacuum Large* and I124-*Uniform* were used to reconstruct phantom P0 while *BtB-Vacuum Large*, I124-*Uniform Large* and I124-*Real Small* were used to reconstruct P1 and P2 phantoms so as to compare the performance of the SM when calculated from about the same number of prompts.

Random coincidences were not included in the computation of the SMs, and only coincidences involving two γ-photons (annihilation-γ or cascade-γ) emitted from the same event were used for SM computation.

A standard Siddon ray-tracing algorithm (Siddon 1985) was also implemented for comparison purpose, where each SM element R_{ij} was proportional to the line intersection between LOR i and voxel j.

Table 1. Number of detected prompts used for each system matrix, taking symmetries into account.

System Matrix	Size (Go)	Number of prompt coincidences
BtB-Vacuum Small	0.3	1.45×10^9
BtB-Vacuum Medium	0.7	8.61×10^9
BtB-Vacuum Large	1.2	2.78×10^{10}
I124-*Uniform Small*	2.1	7.31×10^9
I124-*Uniform Medium*	4.9	1.94×10^{10}
I124-*Uniform Large*	6.8	2.85×10^{10}
I124-*Real XX Small*	2.9	1.18×10^{10}
I124-*Real X Small*	4.6	2.07×10^{10}
I124-*Real Small*	6.2	2.95×10^{10}
I124-*Real Medium*	12.3	6.49×10^{10}
I124-*Real Large*	17.6	9.77×10^{10}

2.4. Reconstruction

The MLEM (Shepp and Vardi 1982) reconstruction algorithm was implemented using a histogrammed LOR-MLEM approach accounting for all symmetries mentioned in section 2.3:

$$f_j^{k+1} = f_j^k \frac{1}{\sum_i^I Rij} \sum_i^I Rij \frac{\mathrm{LOR}i}{\sum_j^J Rij.f_j^k} \tag{1}$$

where f_j^{k+1} is the reconstructed activity in voxel j for iteration $k+1$, f_j^k is the reconstructed activity in voxel j for iteration k, J is the total number of initial voxels, I is the total number of non-zero element related to voxel j, and $(k+1)$ the current iteration.

2.5. Figures of merit

2.5.1. System matrix. The accuracy and statistical quality of an SM calculated using MC simulations are two key factors for reliable image reconstruction. The accuracy depends on the description of the physics processes used for SM computation. The statistical quality is related to the number of simulated events for SM computation.

We defined four figures of merit (FOM) related to the SM:

- *%NonZero:* percent number of non-zero SM elements;
- *%Ones*: percent number of non-zero SM elements computed with only one detected prompt;
- *Pmin, Pmax:* the minimal (non-zero) and maximal probability in the SM, respectively.

The sensitivity images (that intrisically takes into account the medium heterogeneities) were also analyzed for each MC-based SM. Profiles through the central slice of the sensitivity images were drawn to analyze the main differences between the SM.

2.5.2. Reconstructed images. The contrast recoveries for the hot and cold regions were defined as:

$$\mathrm{CR_{Hot}} = 100 \frac{(C_H - C_B)/C_B}{(A_H - A_B)/A_B} = 100 \frac{C_H - C_B}{3C_B} \tag{2}$$

$$\mathrm{CR_{Cold}} = 100\frac{C_B - C_C}{C_B} \tag{3}$$

For P0, C_H, C_C and C_B were respectively the average counts in the hot region, in the cold region and in the background, and A_H and A_B the real average activity in the hot region and the background respectively.

For P2, C_H was the number of counts in the voxel with the highest signal in a 'tumor', according to the NEMA NU-4 recommendations (National Electrical Manufacturers Association 2008).

A profile throughout the hot region (green arrow in figure 2(*b*)) was drawn for phantom P1. Using I124-*Uniform* SM, absolute activity recovery for P0 projections was calculated as:

$$\mathrm{AR_{ROI}} = 100\frac{A_{\mathrm{ROI}}^{\mathrm{Measured}}}{A_{\mathrm{ROI}}^{\mathrm{Theoric}}} \tag{4}$$

where $A_{\mathrm{ROI}}^{\mathrm{Measured}}$ is the reconstructed mean activity per voxel and $A_{\mathrm{ROI}}^{\mathrm{Theoric}}$ the mean activity simulated per voxel in the ROI. Similarly, activity recovery (AR) was also calculated in the five hot regions of P2 when using I124-*Real* SMs.

The average residual activity in cold regions (water and lung) for P2 was compared to the mean activity within the background using:

$$A_{\mathrm{Cold}} = 100\frac{\sum_{j}^{\mathrm{Cold\,ROI}} C(j)\Big/_{J}}{\sum_{k}^{\mathrm{Background}} C(k)\Big/_{K}} \tag{5}$$

where $C(j)$ and $C(k)$ are respectively the value of voxel j in the cold region (lung or water) and of voxel k in the background and J and K are the total number of voxel in those regions.

Last, the coefficient of variation was used as a surrogate of the noise level as follows:

$$\mathrm{CV} = 100\frac{\sigma}{CB} \tag{6}$$

where σ is the standard deviation measured in the background.

The computation time required for each SM was reported.

3. Results

3.1. Characteristics of the system matrices

The SMs were compared according to the total number of prompts used to generate them. Figure 3(*a*) shows the percentage of non-zero entries (*%NonZero*) in all SMs. It can be seen that *BtB-Vacuum* SMs are more sparse than I124 SMs. Moreover, the *%NonZero* for I124 SMs increases linearly with respect to the number of simulated prompts with a higher slope than the one found for *BtB-Vacuum* SMs. The *%Ones* for each SM (figure 3(*b*)) shows that for I124 *SMs*, the large majority of non-zero elements are computed only from one detected prompt compared to *BtB-Vacuum* SMs, and slightly increases with the number of detected prompts. Conversely, *%Ones* decreases with the number of detected prompts in the case of *BtB-Vacuum* SMs.

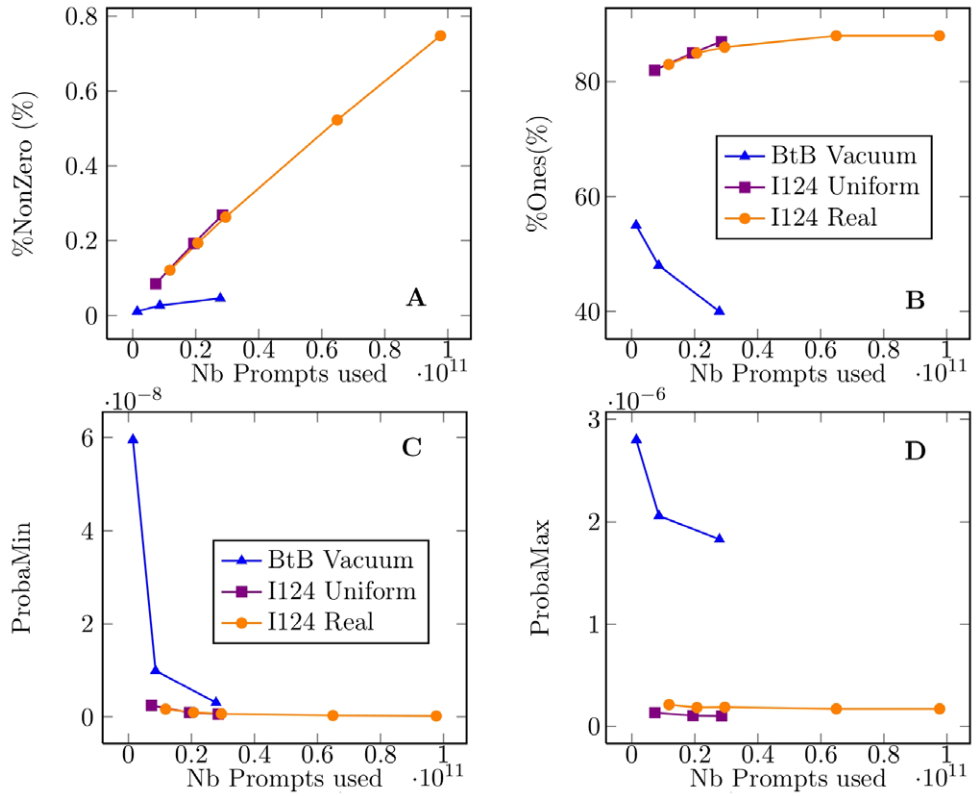

Figure 3. Number of non-zero SM elements (*a*), number of non-zero SM elements computed from only one detected prompt (*b*), and minimum (*c*) and maximum (*d*) probabilities as a function of the number of prompts used for computing each SM.

The minimum (figure 3(*c*)) and maximum (figure 3(*d*)) probabilities show that the probabilities computed for each I124 SMs are lower than those of *BtB-Vacuum* SMs, with a flat trend with respect to the detected number of prompts.

Figure 4 shows the profiles through the different sensitivity images for each SM computed by Monte Carlo. The strong impact of modelling the positron range can be clearly seen in the sensitivity image as a function of density heterogeneities while the profile of the *BtB-Vacuum* SM sensitivity image has a conventional shape in agreement with results reported by Aguiar *et al* (2010).

3.2. Image quality

3.2.1. Homogeneous P0 phantom. In the case of a homogeneous medium, for the same number of prompts used for calculating the SMs, the *BtB-Vacuum* and I124-*Uniform* SMs yielded a better contrast recovery for the hot and cold regions (figure 5) compared with a Siddon-based SM. Modelling the attenuation medium increased the contrast recovery compared to data reconstructed with *BtB-Vacuum* SM.

The absolute activity recoveries were 99 and 101% for the hot region and background respectively (CV = 6%) when using the SM I124-*Uniform Large*, with a number of prompts used to calculate this SM 12 000 times higher than the number of prompts recorded in the

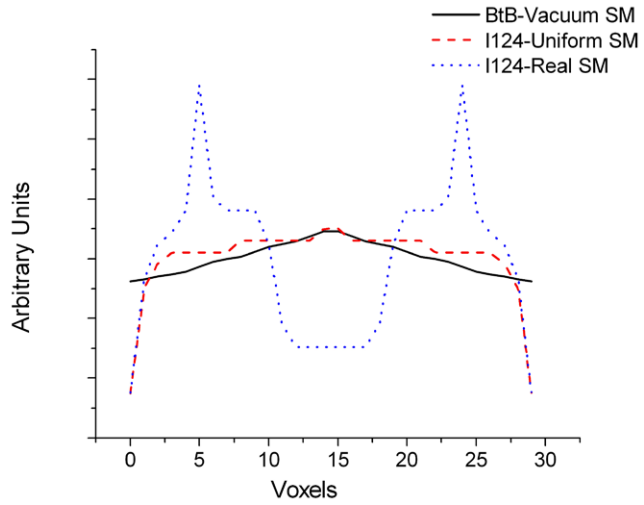

Figure 4. Profiles through the sensitivity images computed with three different Monte Carlo SMs (*BtB-Vacuum Large*, I124-*Uniform Large* and I124-*Real Small*).

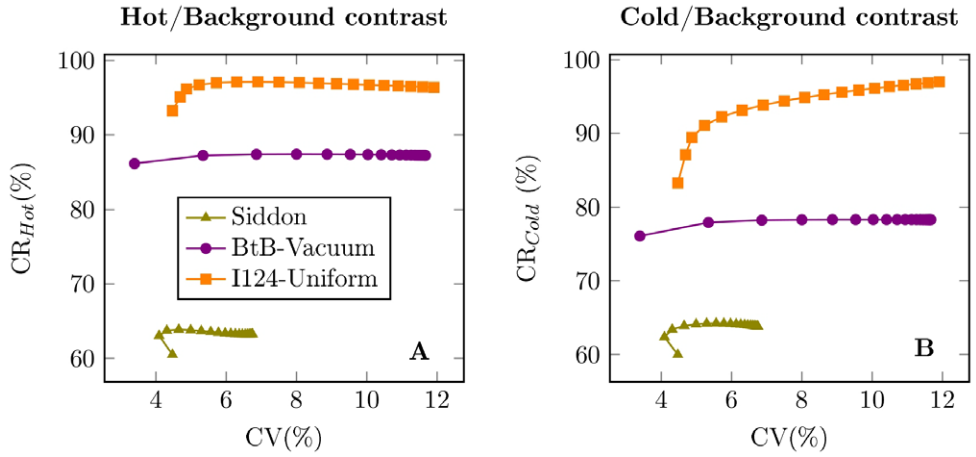

Figure 5. Contrast recovery in the hot (*a*) and cold (*b*) regions of phantom P0 as a function of the coefficient of variation (CV) for three SMs. About the same number of prompts was used for the two Monte Carlo SM (*BtB-Vacuum Large*, I124-*Uniform Large*). Each CV value corresponds to a number of MLEM iteration.

projections. Using the SM I124-*Uniform Small*, activity recovery decreases to 88% within the hot region for the same background noise level.

3.2.2. Heterogeneous phantoms. P1 phantom. Phantom P1 was reconstructed using the four SMs defined in section 2.3. For each SM, the iteration number was chosen so that CV = 12%. The reconstructed images and associated normalized profiles through the hot region are shown in figure 6. Due to the positron range, a high uptake in the bone region (hot and cold) and a low uptake for the hot lung region were observed when using the *BtB-Vacuum* SM and Siddon algorithm. These artifacts were reduced when using the I124-*Real* SM. Only the use of the

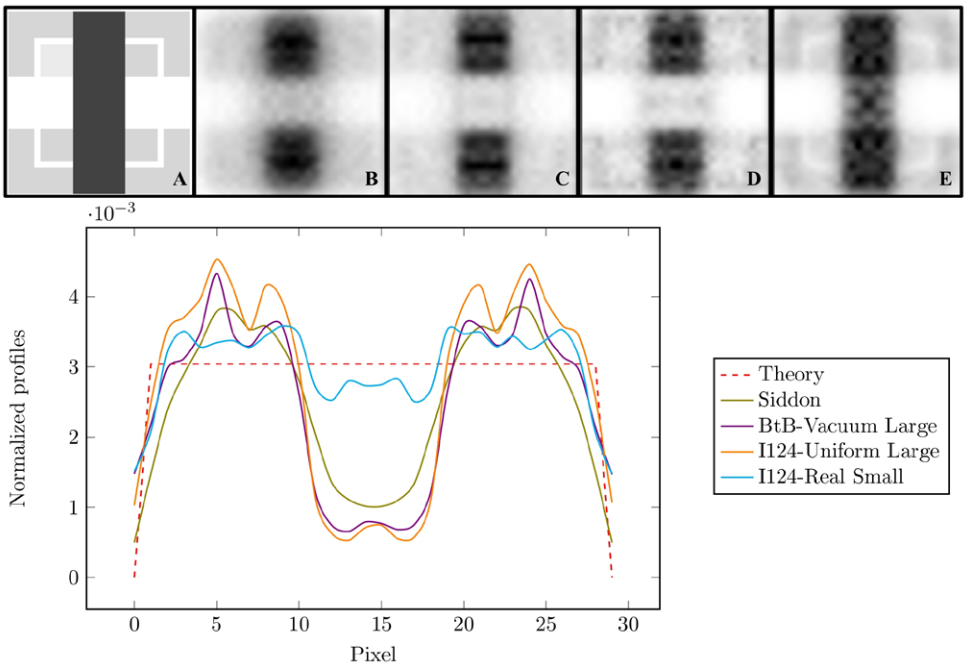

Figure 6. Top: reconstructed images of P1 (CV = 12%) with four SMs: (*b*) Siddon, (*c*) *BtB-Vacuum Large*, (*d*) I124-*Uniform Large* and (*e*) I124-*Real Small* (about the same number of prompt coincidences was used for computing the three Monte Carlo SM), compared to the theoretical distribution (*a*). Gray-scale is identical for all images. Bottom: Line profiles through the hot region of P1 phantom (see profile location in figure 2 (*b*)). Profiles were normalized by the total number of reconstructed counts in each image.

I124-*Real* SM with a precise modelling of the propagating medium allowed partial recovery of activity in the lung region (92%).

P2 phantom. P2 phantom was reconstructed using the four SMs described in section 2.3. For each SM, the iteration number was chosen so that CV = 6%. Reconstructed images are shown in figure 7. The contrast recovery for the smallest region ($1 \times 1\,\text{mm}^2$) was not reported as it was not distinguishable from the background.

The hot region contrasts were better recovered using the MC SMs regardless the background noise level (figure 8). For 'tumors' between 3 and 5 mm in size, the use of I124-*Uniform* SM improved the contrast recovery compared to *BtB-Vacuum* SM. The contrast recovery tended to be higher when using I124-*Uniform* SM (except for the largest tumor) than using the I124-*Real* SM.

Unlike the other MC SMs, the I124-*Real* SM failed to properly identify the cold lung region (figure 8(*f*)). The contrast in the cold water region was better recovered when using I124-*Uniform* and I124-*Real* SMs than with the Siddon and *BtB-Vacuum* SMs (figure 8(*e*)). Finally, it was more challenging to identify the absence of activity in the cold lung region than in the cold water region.

The impact of the number of detected prompts used for computing the I124-*Real* SM is illustrated in figures 8 and 9. Increasing the number of prompts used to compute the SM

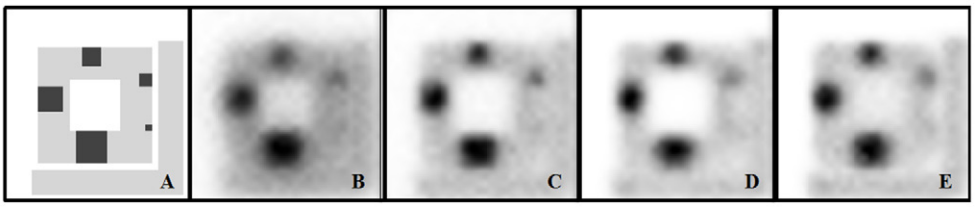

Figure 7. Reconstructed images of P2 phantom (CV = 6%) for four SMs: (*b*) Siddon, (*c*) *BtB-Vacuum Large*, (*d*) I124-*Uniform Large* and (*e*) I124-*Real Small* (about the same number of prompts was used for computing the three Monte Carlo SMs), compared to the theoretical distribution (*a*). Gray-scale is identical for all images.

yielded a better absolute activity recovery for all 'tumors' and for the cold lung region (figures 8(*a*)–(*f*) and figures 9(*a*)–(*d*) and (*f*)). The lack of activity in the cold water region was properly identified whatever the SM (figure 9(*e*)).

Table 2 shows the computation time needed for each SM computation.

4. Discussion

We developed and assessed a fully 3D MC reconstruction method for ^{124}I preclinical PET. Three different types of system matrices (SMs) were computed to study the impact of different levels of complexity and statistical properties. The first level of complexity was to simulate the PET system response using the *BtB-Vacuum* model. Then the model was refined by including the positron range and the spurious coincidences when particles propagated in a uniform medium (I124-*Uniform* SM). This intermediate step was chosen since it can be used regardless of the exact description of the propagation medium, for instance when no transmission scan is available. Finally, a full and complete description of the physics processes for computing the SM was used (I124-*Real SM*). As the SMs are calculated using the MC approach involving simulating a fixed number of possible particle histories, each SM entry is noisy. There is therefore a trade-off between the sophistication of the model (yielding many different particle trajectories) and the noise in each entry estimate.

Figure 3 shows that it is more challenging to get entries with low noise for the I124 SMs compared with *BtB-Vacuum* SMs. Indeed, for a given number of simulated prompts, accounting for all the physics processes (positron range, scattered and spurious coincidences) lead to a larger number of possible LOR through each voxel, which increases the total number of SM entries. These results are consistent with conclusions reported by other groups (Rafecas *et al* 2004, Cabello and Rafecas 2012). We also found that for I124 SMs, most non-zero entries were calculated only from a single detected event, involving a high statistical variance compared to *BtB-Vacuum* SMs entries.

As a result, the number of prompts used to calculate the SM plays an essential role and should be as high as possible when using a sophisticated description of the physics processes. As an example, a decrease of 13% in contrast recovery was observed when four times less coincidences were used to compute the I124-*Uniform Small* SM for P0. In P0, the number of prompts used to calculated the I124-*Uniform* SM has to be 12 000 times higher than the number of prompts recorded in the projections to achieve a contrast recovery higher than 99% in the background and in the hot region. Results presented in figures 8 and 9 advocate for the need to reduce the variance of the SM for achieving better quantitative results when using an SM that fully models the physics processes. With the most accurate I124-*Real* SM, absolute activity recovery was always higher than 85% for all structures larger than 2 mm (figure 9).

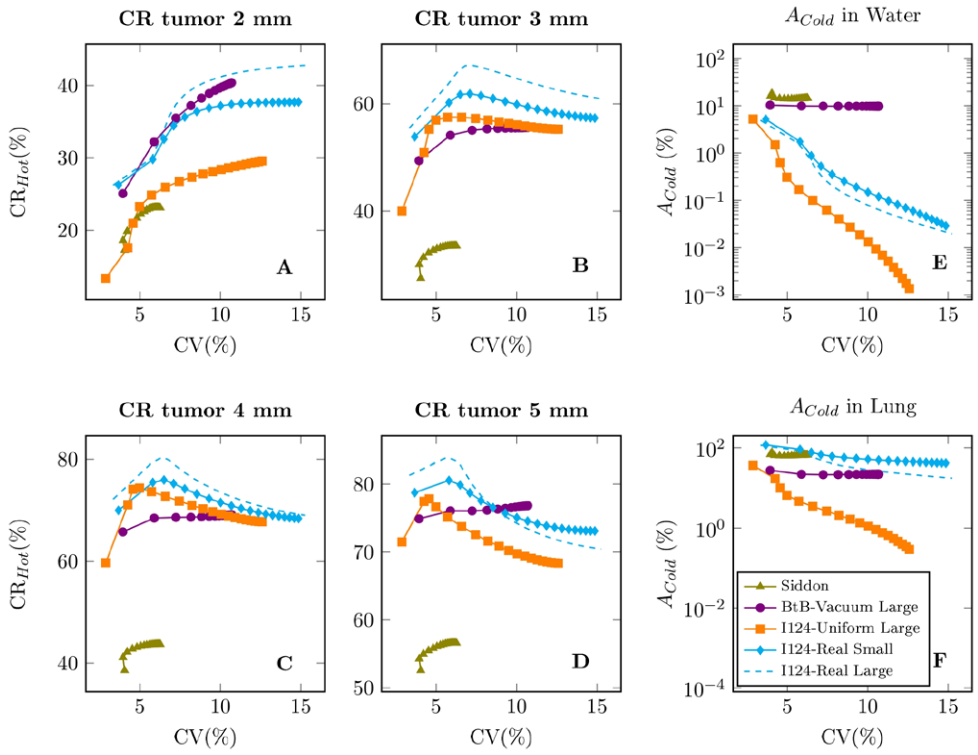

Figure 8. Contrast recovery for various tumors (P2 phantom, tumors size are: 2 mm (*a*), 3 mm (*b*), 4 mm (*c*) and 5 mm (*d*)) and average percentage of residual activity in cold regions (*e*): water, (*f*): lung) as a function of CV for four SMs. About the same number of prompt coincidences was used for computing the Monte Carlo SM (*BtB-Vacuum Large*, I124-*Uniform Large* and I124-*Real Small*). Results when using I124-*Real Large* SM are also presented for highlighting the impact of increasing the number of prompts used in the calculation of the most sophisticated SM.

However, it is worth mentioning that increasing the simulated number of prompts has obviously a significant cost in term of computation time.

Using I124-*Uniform* or I124-*Real* SMs allowed a better contrast recovery for hot and cold regions than simply taking into account the PSF in the SM as performed when using the *BtB-Vacuum* SM (figures 5 and 6). *BtB-Vacuum* SM increases the contrast recovery when compared to the use of the Siddon ray-tracing algorithm, but the improvement was found lower than that between *BtB-Vacuum* SMs and I124-*Uniform* SMs (figure 5) or between *BtB-Vacuum* and I124-*Real* SMs (figure 6). A complete modelling of the system (scanner and object) yielded better qualitative and quantitative results compared with the SM *BtB-Vacuum*, with around 50% improvement in contrast recovery for the hot lung and hot bone regions in P1 (figure 6) and 10 and 20% improvement in contrast recovery for the hot and cold regions respectively in P0 (figure 5). Results shown in figure 6 confirm that precisely accounting for the medium heterogeneity (water, lung and bone) for SM computation yields better quantitative results when activity is present in all regions (figure 2(*b*)), compared to the use of PSF only or PSF and soft tissue modelling only. The activity distribution in the object plays an essential role in the identification of the most appropriate SM. As expected, the use of *BtB-Vacuum* and I124-*Uniform* SMs did not make it possible to correctly locate positron decays

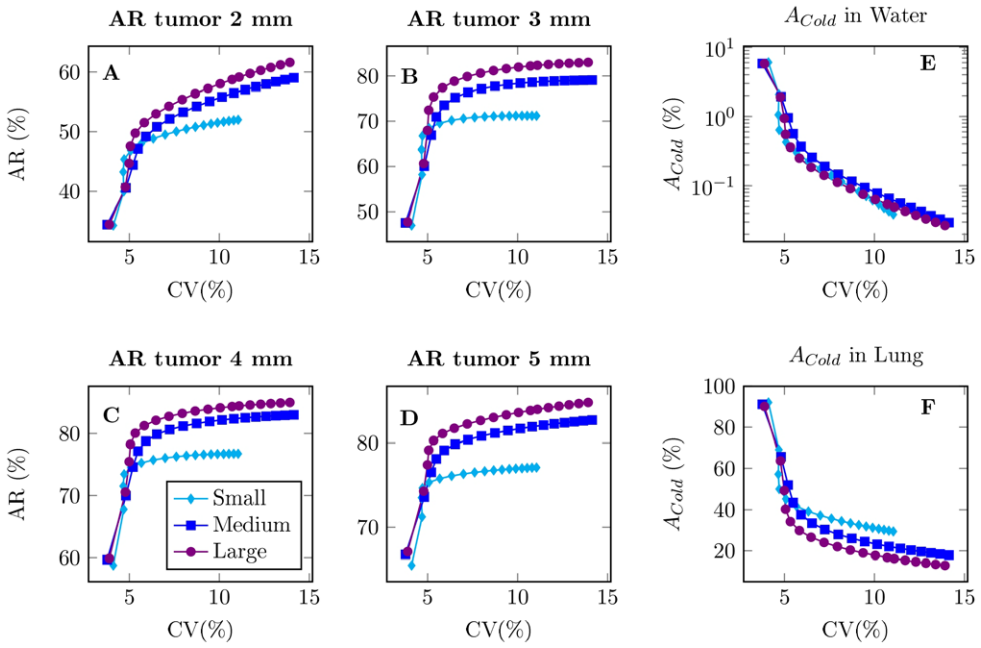

Figure 9. Activity recovery (AR) for various 'tumors' (P2 phantom) (tumors size are: 2 mm (*a*), 3 mm (*b*), 4 mm (*c*) and 5 mm (*d*)) and average percentage residual activity in the cold regions (*e*): water, (*f*): lung) as a function of the CV using the I124-*Real* SMs.

Table 2. Computation time for generating each SM (for one Intel Xeon CPU @ 2.4 GHz).

System Matrix	SM computation time (*h*)
BtB-Vacuum Small	6
BtB-Vacuum Medium	24
BtB-Vacuum Large	72
I124-*Uniform Small*	43
I124-*Uniform Medium*	108
I124-*Uniform Large*	168
I124-*Real Small*	168
I124-*Real Medium*	336
I124-*Real Large*	504

when activity was distributed in regions with large difference in density (lung versus water and bone versus water). The activity was overestimated in bone region while it was underestimated in lung region (figures 6(*c*) and (*d*)) because of the positron range. The impact of modelling all physics processes in the SM was especially visible for the P1 phantom where activity was present in all different media.

With a different activity distribution in the same heterogeneous object (figure 2(*c*)), where activity is only present in water, the reconstructions using MC-based SMs still yielded better contrast recovery than when using SM based on the Siddon ray-tracing algorithm (figure 8). Yet, using the I124-*Real* SM decreased the contrast recovery for all 'tumors' (except for the largest) when comparing with data reconstructed with *BtB-Vacuum* or I124-*Uniform* SMs (figure 8). These observations suggest that the use of SM that account for the different density

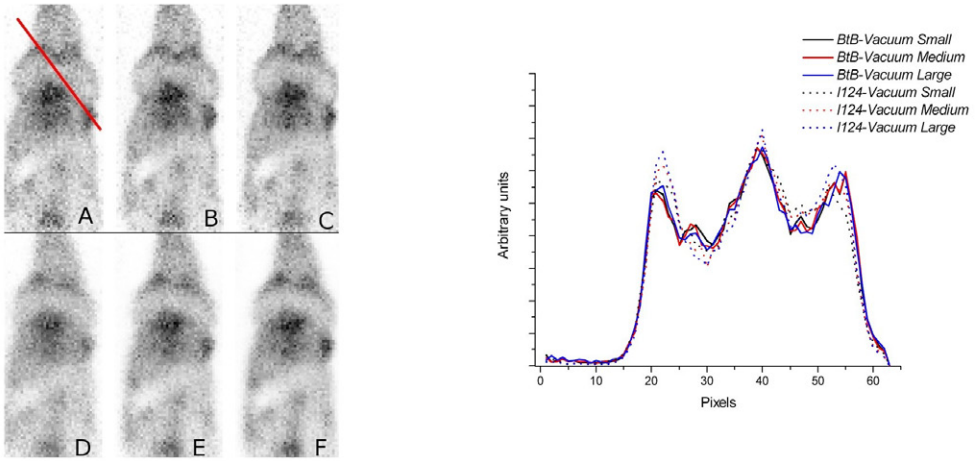

Figure 10. Reconstructed images using the *BtB-Vacuum* (*a*, *b*, *c*) and the I124-*Uniform* (*d*, *e*, *f*) SMs for a mouse that over-expressed CD138 in a breast carcinoma model injected with 3.5 MBq of 124I-labeled B–B4 mAb. Small (*a*, *d*), medium (*b*, *e*) and large (*c*, *f*) SMs have been used. Left: profiles through the red line shown in (*a*).

in the object did not necessarily lead to more accurate quantitative results compared to using an SM that assumed a uniform medium. In this case, for the same number of prompt coincidences used to compute all MC-based SMs, using the SM that precisely modeled the particle interactions within the scanner and the object can worsen the quantitative results compared to a less sophisticated SM because of insufficient statistics when calculating the most complex SM (figures 8(*a*)–(*c*)). However, the respective performance of the SM also highly depends on the activity and attenuation distributions of the object to be reconstructed (see supplemental data) (stacks.iop.org/PMB/60/062475) and makes very difficult to derive a general rule given a fixed number of prompt coincidences used for computing each SM.

We also noted that the smallest structure (e.g. 2 mm size, figure 8(*a*)) was more challenging to recover when the complexity of the SM increased (from *BtB-Vacuum* to I124-*Real*). This might be due to the fact that a small structure is present in a small number of voxels that are crossed by a higher number of LOR in I124-*Uniform* or I124-*Real* SM calculation compared to the ray-tracing algorithm or even the *BtB-Vacuum* SM), yielding many SM elements with high variance that complicate image reconstruction.

This work also suggests that the presence of low-density regions (e.g. lung) makes it even more difficult to get SM entries with a low variance compared to a phantom with a uniform medium of higher density. In the case of a cold lung region for example, the use of I124-*Real* SM actually decreased contrast recovery compared to the use of other MC-based SMs that do not account for those low density regions (figures 7 and 8(*f*)). Indeed, during the SM calculation, positron starting from a voxel located in a low-density region may be detected in a high number of LOR given their higher mean free path compared to their mean free path in a water region. For a same number of simulated decay per voxel used to compute the SM entries, the SM element variance associated to those voxels is thus higher than those computed for voxels located in water.

For illustration purpose only, figure 10 shows an application of the developed approach in a real pre-clinical setting using the high-resolution small animal Inveon PET system, demonstrating the practical feasibility of the approach.

Last, the SM computation times reported in table 2 suggest that without any optimization, the use of the proposed approach is still of limited interest. For the real mouse example shown in figure 10, 16 d (using 336 Intel Xeon CPUs @ 2.4 GHz) were needed for the I124-*Uniform Large* SM calculation (figure 10(*f*)). Yet, several strategies could be used to reduce computation time, including taking advantage of GPU as proposed in GATE v7.0.

5. Conclusion

We developed a fully 3D MC system matrix computation and reconstruction method for ^{124}I preclinical PET acquisitions. The trade-off between complexity (i.e. modelling all physics processes) and statistical robustness for the SM computation was studied. When activity was distributed in regions with different densities, only a precise modelling of the object made it possible to recover hot and cold regions with a maximum deviation in activity estimates of +/ − 20%. However, in a realistic case when activity was present only in soft tissue within a heterogeneous propagation medium, the use of an SM that fully modelled all physics processes in the object and in the PET scanner did not always improved the activity recovery. An SM that only accounted for particle propagation in soft tissue and for the system PSF yielded the most accurate results due to the lack of sufficient statistics in the most sophisticated SM modelling the different densities in the object.

Acknowledgments

The authors wish to thank Dr Simon Stute for valuable discussion. This work was supported by a grant from the Pays de la Loire Council called ‘Nucléaire pour la Santé’ (NucSan).

References

Aguiar P, Pino F, Silva-Rodríguez J, Pavía J, Ros D, Ruibal Á and El Bitar Z 2014 Analytical, experimental, and Monte Carlo system response matrix for pinhole SPECT reconstruction *Med. Phys.* **41** 032501

Aguiar P, Rafecas M, Ortuño J E, Kontaxakis G, Santos A, Pavía J and Ros D 2010 Geometrical and Monte Carlo projectors in 3D PET reconstruction *Med. Phys.* **37** 5691–702

Alessio A and MacDonald L 2008 Spatially variant positron range modelling derived from CT for PET image reconstruction *IEEE Nuclear Science Symp. Conf. Rec.* (*Dresden Germany, 19–25 October 2008*) pp 3637–40

Bai B, Laforest R, Smith A M and Leahy R M 2005 Evaluation of MAP image reconstruction with positron range modelling for 3D PET *IEEE Nuclear Science Symp. Conf. Rec.* (*Fajardo, 23–29 October 2005*) vol 5 pp 2686–89

Bai B, Ruangma A, Laforest R, Tai Y-C and Leahy R M 2003 Positron range modelling for statistical PET image reconstruction *IEEE Nuclear Science Symp. Conf. Rec.* (*Portland, 19–25 October 2003*) vol 4 pp 2501–5

Beattie B J, Finn R D, Rowland D J and Pentlow K S 2003 Quantitative imaging of bromine-76 and yttrium-86 with PET: a method for the removal of spurious activity introduced by cascade gamma rays *Med. Phys.* **30** 2410–23

Cabello J and Rafecas M 2012 Comparison of basis functions for 3D PET reconstruction using a Monte Carlo system matrix *Phys. Med. Biol.* **57** 1759–77

Cal-González J, Herraiz J K, España S, Desco M, Vaquero J J and Udías J M 2009 Positron range effects in high resolution 3D PET imaging *IEEE Nuclear Science Symp. Conf. Rec.* (*Orlando, FL, 24 October–1 November 2009*) pp 2788–91

Cecchetti M, Moehrs S, Belcari N and Del Guerra A 2013 Accurate and efficient modelling of the detector response in small animal multi-head PET systems *Phys. Med. Biol.* **58** 6713–31

Cheng J C, Agbeko N, O'Sullivan J and Laforest R 2009 Evaluation of an iterative cascade gamma ray correction algorithm for non-standard PET nuclides at various counting statistics in high resolution small animal PET imaging *IEEE Nuclear Science Symp. Conf. Rec.* (*Orlando, FL, 24 October–1 November 2009*) pp 2842–5

Cheng J C and Laforest R 2011 Incorporation of a cascade gamma ray correction into the SRW iterative reconstruction for non-standard PET nuclides: towards a unified correction weighted (UCW) scheme in the sensitivity image *IEEE Nuclear Science Symp. Conf. Rec.* (*Valencia, 23–29 October 2011*) pp 4059–62

Disselhorst J, Brom M, Laverman P, Slump C, Boerman O, Oyen W, Gotthardt M and Visser E 2010 Image-quality assessment for several positron emitters using the NEMA NU 4-2008 standards in the siemens inveon small-animal PET scanner *J. Nucl. Med.* **51** 610–7

Floyd C E, Jaszczak R J, Greer K L and Coleman R E 1986 Inverse Monte Carlo as a unified reconstruction algorithm for ECT *J. Nucl. Med.* **27** 1577–85

Fu L and Qi J 2010 A residual correction method for high-resolution PET reconstruction with application to on-the-fly Monte Carlo based model of positron range *Med. Phys.* **37** 704–13

Gregory R A, Hooker C A, Partridge M and Flux G D 2009 Optimization and assessment of quantitative 124I imaging on a Philips gemini dual GS PET/CT system *Eur. J. Nucl. Med. Mol. Imag.* **36** 1037–48

Herbertson R A *et al* 2014 Targeted chemoradiation in metastatic colorectal cancer: a phase I trial of ^{131}I-huA33 with concurrent capecitabine *J. Nucl. Med.* **55** 534–9

Herzog H, Tellmann L, Scholten B, Coenen H H and Qaim S M 2008 PET imaging problems with the non-standard positron emitters Yttrium-86 and Iodine-124 *Q. J. Nucl. Med. Mol. Imag.* **52** 159–65

Herzog H, Tellmann L, Qaim S M, Spellerberg S, Schmid A and Coenen H H 2002 PET quantitation and imaging of the non-pure positron-emitting iodine isotope 124I *Appl. Radiat. Isot.* **56** 673–9

Jan S *et al* 2011 GATE V6: a major enhancement of the GATE simulation platform enabling modelling of CT and radiotherapy *Phys. Med. Biol.* **56** 881–901

Jentzen W 2010 Experimental investigation of factors affecting the absolute recovery coefficients in iodine-124 PET lesion imaging *Phys. Med. Biol.* **55** 2365–98

Johnson C A, Yan Y C, Carson R E, Martino R L and Daube-Witherspoon M E 1995 A system for the 3D reconstruction of retracted-septa PET data using the EM algorithm *IEEE Trans. Nucl. Sci.* **42** 1223–7

Knowles S M and Wu A M 2012 Advances in immuno-positron emission tomography: antibodies for molecular imaging in oncology *J. Clin. Oncol.* **30** 3884–92

Kontaxakis G, Strauss L G, Thireou T, Ledesma-Carbayo M J, Santos A, Pavlopoulos S A and Dimitrakopoulou-Strauss A 2002 Iterative image reconstruction for clinical PET using ordered subsets, median root prior and a web based interface *Mol. Imag. Biol.* **4** 219–31

Kull T, Ruckbager J, Weller R, Reske S and Glatting G 2004 Quantitative imaging of yttrium-86 PET with the ECAT EXACT HR + in 2D mode *Cancer Biother. Radiopharm.* **19** 482–90

Laforest R and Liu X 2009 Cascade removal and microPET imaging with 76Br *Phys. Med. Biol.* **54** 1503–31

Lazaro D, El Bitar Z, Breton V, Hill D and Buvat I 2005 Fully 3D Monte Carlo reconstruction in SPECT: a feasibility study *Phys. Med. Biol.* **50** 3739–54

Lubberink M, Schneider H, Bergström M and Lundqvist H 2002 Quantitative imaging and correction for cascade gamma radiation of 76Br with 2D and 3D PET *Phys. Med. Biol.* **47** 3519–34

Lütje S, Rijpkema M, Franssen G M, Fracasso G, Helfrich W, Eek A, Oyen W J, Colombatti M and Boerman O C 2014 Dual-modality image-guided surgery of prostate cancer with a radiolabeled fluorescent anti-PSMA monoclonal antibody *J. Nucl. Med.* **55** 995–1001

National Electrical Manufacturers Association 2008 Performance measurements for small animal positron emission tomographs NEMA Standards Publication NU 4-2008

Ortuño J E, Kontaxakis G E, Rubio J L, Guerra P and Santos A 2010 Efficient methodologies for system matrix modelling in iterative image reconstruction for rotating high-resolution PET *Phys. Med. Biol.* **55** 1833–61

Pentlow K S, Finn R D, Larson S M, Erdi Y E, Beattie B J and Humm J L 2000 Quantitative imaging of Yttrium-86 with PET. The occurrence and correction of anomalous apparent activity in high density regions *Clin. Positron Imag.* **3** 85–90

Poli G L, Bianchi C, Virotta G, Bettini A, Moretti R, Trachsel E, Elia G, Giovannoni L, Neri D and Bruno A 2013 Radretumab radioimmunotherapy in patients with brain metastasis: a 124I-L19SIP dosimetric PET study *Cancer Immunol. Res.* **1** 134–43

Qi J Y, Leahy R M, Cherry S R, Chatziioannou A and Farquhar T H 1998 High-resolution 3D Bayesian image reconstruction using the MicroPET small-animal scanner *Phys. Med. Biol.* **43** 1001–13

Rafecas M, Mosler B, Dietz M, Pögl M, Stamatakis A, McElroy D and Ziegler S 2004 Use of a Monte Carlo-based probability matrix for 3D iterative reconstruction of MADPET-II data *IEEE Trans. Nucl. Sci.* **51** 2597–605

Rahmim A, Qi J and Sossi V 2013 Resolution modelling in PET imaging: theory, practice, benefits, and pitfalls *Med. Phys.* **40** 064301–16

Rahmim A, Tang J, Lodge M A, Lashkari S, Ay M R, Lautamäki R, Tsui B M W and Bengel F M 2008a Analytic system matrix resolution modelling in PET: an application to Rb-82 cardiac imaging *Phys. Med. Biol*. **53** 5947–65

Rahmim A, Tang J, Lodge M A, Lashkari S, Ay M R and Bengel F M 2008b Resolution modeled PET image reconstruction incorporating space-variance of positron range: Rb-82 cardiac PET imaging *IEEE Nuclear Science Symp. Conf. Rec.* (*Dresden, Germany, 19–25 October 2008*) pp 3643–50

Ruangma A, Bai B, Lewis J S, Sun X, Welch M J, Leahy R and Laforest R 2006 3D maximum a posteriori (MAP) imaging with radiopharmaceuticals labeled with three Cu radionuclides *Nucl. Med. Biol.* **33** 217–26

Sauerzapf S, Thomas L, Behe M, Weber W, Zakhnini A, Pietrzyk A and Mix M 2011 Using Monte-Carlo simulations to implement corrections for I-124 as a non-pure positron emitter in small animal and human PET imaging *IEEE Nuclear Science Symp. Conf. Rec.* (*Valencia, 23–29 October 2011*) pp 2688–91

Shepp L A and Vardi Y 1982 Maximum likelihood reconstruction for emission tomography medical imaging *IEEE Trans. Med. Imaging* **1** 113–22

Siddon R L 1985 Fast calculation of the exact radiological path for a three-dimensional CT array *Med. Phys.* **12** 252–5

Surti S, Scheuermann R and Karp J S 2009 Correction technique for cascade gammas in I-124 imaging on a fully-3D, time-of-flight PET scanner *IEEE Trans. Nucl. Sci.* **56** 653–60

Taleb D, Ali Bahri M, Warnock G, Salmon E, Luxen A, Plenevaux A, Anizan N and Seret A 2012 performance measurements of the microPET FOCUS 120 for iodine-124 imaging *IEEE Trans. Nucl. Sci.* **59** 1868–78

Vandenberghe S, Staelens S, Byrne C L, Soares E J, Lemahieu I and Glick S J 2006a Reconstruction of 2D PET data with Monte Carlo generated system matrix for generalized natural pixels *Phys. Med. Biol*. **51** 3105–25

Vandenberghe S 2006b 3D positron emission tomography imaging with 124I and 86Y *Nucl. Med. Commun.* **27** 237–45

Veklerov E, Llacer J and Hoffman E J 1988 MLEM reconstruction of a brain phantom using a Monte Carlo transition matrix and a statistical stopping rule *IEEE Trans. Nucl. Sci.* **35** 603–7

Walrand S, Jamar F, Mathieu I, De Camps J, Lonneux M, Sibomana M, Labar D, Michel C and Pauwels S 2003 Quantitation in PET using isotopes emitting prompt single gammas: application to yttrium-86 *Eur. J. Nucl. Med. Mol. Imag.* **30** 354–61

Walte A, Sriyapureddy S S, Korkmaz Z, Krull D, Bolte O, Hofmann M, Meyer G J and Knapp W H 2007 Preparation and evaluation of 211At labelled antineoplastic antibodies *J. Pharm. Pharm. Sci.* **10** 277s–85s

Watson C C 2000 New, faster, image-based scatter correction for 3D PET *IEEE Trans. Nucl. Sci.* **47** 1587–94

Wright B D and Lapi S E 2013 Designing the magic bullet? the advancement of immuno-PET into clinical use *J. Nucl. Med.* **54** 1171–4

Yao R, Balakrishnan S, Ambwani S, Rathod V and Shao Y 2005 Quantitative Iodine-124 Imaging on animal PET *IEEE Nuclear Science Symp. Conf. Rec*. (*Fajardo, 23–29 October 2005*) vol 3, pp 1649–52

Yu A R, Kim J S, Kim K M, Lee Y S, Woo S K, Lee W H, Kim J G, Park J A, Kim H J and Cheon G J 2009 Optimal PET acquisition setting of I-124 with siemens inveon PET: comparative simulation study with F-18 and microPET R4 *IEEE Nuclear Science Symp. Conf. Rec.* (*Orlando, FL, 24 October–1 November 2009*) pp 2666–8